Magnetism and phase structure of crystallized Sm–Fe–B melt spun ribbons

2002 J. Phys.: Condens. Matter 14 12599

(http://iopscience.iop.org/0953-8984/14/47/331)

INSTITUTE OF PHYSICS PUBLISHING JOURNAL OF PHYSICS: CONDENSED MATTER

J. Phys.: Condens. Matter **14** (2002) 12599–12609 PII: S0953-8984(02)38925-2

Magnetism and phase structure of crystallized Sm–Fe–B melt spun ribbons

O Crisan[1,5], J M Le Breton[2], M Noguès[3], F Machizaud[4] and G Filoti[1]

[1] National Institute for Materials Physics, PO Box MG-7, 76900 Bucharest, Romania
[2] GPM, UMR 6634 CNRS, Université de Rouen, 76801 Saint Etienne du Rouvray Cedex, France
[3] LMOV, CNRS-Université de Versailles, 78035 Versailles Cedex, France
[4] LSG2M, UMR CNRS 7584, Université de Nancy, 54042 Nancy Cedex, France

E-mail: crisan@physics.auth.gr

Received 7 July 2002
Published 15 November 2002
Online at stacks.iop.org/JPhysCM/14/12599

Abstract

The crystallization of amorphous $Sm_xFe_{80-x}B_{20}$ melt spun ribbons is studied over an extended range of composition ($0 < x < 8$). Differential scanning calorimetry scans reveal different endo- and exothermic effects depending upon the composition. X-ray diffraction and Mössbauer studies for samples annealed at temperatures close to the onset of the first exothermic effect prove that, during the primary crystallization of the amorphous ribbons, both α-Fe and Fe_3B phases appear—with Sm ions randomly accommodating the Fe sites in the tetragonal Fe_3B lattice—while the subsequent exothermic reactions correspond to the decomposition of the metastable Fe_3B phase into α-Fe and Fe_2B and to the formation of the ternary $Sm_{1.1}Fe_4B_4$ phase. Fully crystallized ribbons with Sm contents lower than about 7 at.% show the co-existence between α-Fe and Fe_2B soft magnetic phases and the $Sm_2Fe_{14}B$ magnetic one. The enhancement of magnetic properties with increasing relative proportion of magnetic phase is discussed and correlated with exchange coupling and spin wave stiffness data obtained from the magnetic measurements.

1. Introduction

The ternary RE–Fe–B alloys (RE = rare earth) obtained in the amorphous state by melt-spinning and subsequent annealing have been extensively studied since new and outstanding magnetic properties, compared with conventional permanent magnets, were predicted [1, 2]. The enhanced remanence and coercivity of this type of material are related to the interphase exchange coupling within the composite system. The hard magnetic grains—most commonly

[5] Address for correspondence: Aristotle University of Thessaloniki, Department of Physics, 54124 Thessaloniki, Greece.

$RE_2Fe_{14}B$—are magnetically coupled through the soft magnetic ones—such as α-Fe or Fe_3B—if the size of the soft magnetic regions is in the range of the exchange–correlation length. Change of the alloy composition may promote different intermediate metastable phases during the annealing treatment and consequently, the resulting phase structure would be different. In the case of $RE_xFe_{80-x}B_{20}$ amorphous ribbons, several studies [3–5] have shown that the crystallization temperature of the amorphous ribbons increases with the RE content up to a critical value x_c of about 7 at.% and decreases for higher RE content. This behaviour has been assigned to a modification of the local order of the amorphous ribbons around x_c [4]. In a previous work [5] we have reported on the crystallization processes and the phase microstructure of fully crystallized $Sm_xFe_{80-x}B_{20}$ ribbons. We have shown that below the critical Sm content $x_c = 7.2$ at.% the crystallization of the $Sm_2Fe_{14}B$ magnetic phase together with the α-Fe and Fe_2B phases is promoted, while above x_c both $Sm_{1.1}Fe_4B_4$ and α-Fe phases are preponderant. The nature of the intermediate metastable phases that appear during the crystallization of RE–Fe–B ribbons and lead to different crystallization products still remains a controversial issue, being strongly related to the local chemical composition of the ribbons.

In the present study, we report on the structure and magnetic properties of melt spun ribbons $Sm_xFe_{80-x}B_{20}$ (with $x < x_c$) induced during the crystallization process as well as of the fully crystallized samples. Investigations by x-ray diffraction (XRD), ^{57}Fe Mössbauer spectrometry (MS) and magnetic measurements are detailed.

2. Experimental details

Four $Sm_xFe_{80-x}B_{20}$ amorphous ribbons with $x = 2.4, 4.0, 5.6$ and 7.2 at.% have been produced by the melt-spinning technique in a protective argon atmosphere. The details about the preparation were presented elsewhere [6]. The crystallization process of the as-quenched ribbons was studied by differential scanning calorimetry (DSC) up to 812 °C, using a Setaram DSC 111 system, with a heating rate of 5 K min^{-1}. The samples were investigated by XRD, using a fast curved detector with the Co Kα radiation ($\lambda = 0.179\,09$ nm). Room temperature transmission ^{57}Fe MS measurements of the crystallized ribbons were performed with a conventional set-up using a ^{57}Co source in a Rh matrix. The temperature and field dependence of the magnetization has been obtained using a superconducting quantum interference device (SQUID) in a temperature range of 5–300 K under an applied field up to 5.5 T parallel to the ribbon plane.

3. Results and discussions

3.1. Crystallization process

The composition of the as-quenched ribbons, as determined by energy dispersion spectroscopy (EDS), and the different annealing conditions are shown in table 1.

The DSC scans are typical for amorphous RE–TM–B ribbons. The curve obtained for the sample with Sm content $x = 4.0$ at.% (figure 1, upper curve) exhibits firstly a single weak exothermic peak corresponding to the onset of crystallization (T_{onset}), and a highly intense exothermic peak, which corresponds to the bulk crystallization of the ribbon (T_{cryst}). One or two supplementary exothermic peaks corresponding to phase transformations of the primary crystallization products (T_2 and T_3) may also occur, depending on the chemical composition of the ribbons. For the case of the sample with Sm content $x = 7.2$ at.% (figure 1, lower curve) the onset of crystallization is shown by the continuous increase of the heat flow before onset of the main exothermic peak and only one supplementary exothermic peak, corresponding to the

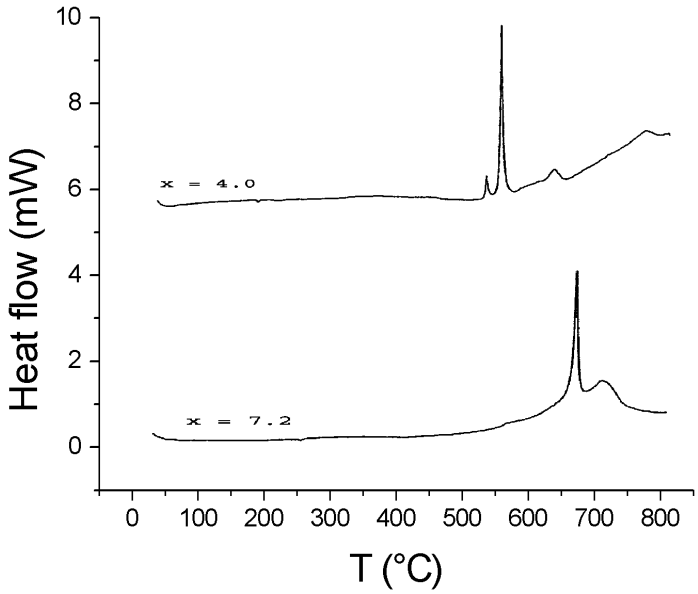

Figure 1. The DSC scan for the $x = 4.0$ and 7.2 at.% Sm amorphous ribbons.

Table 1. Composition of the as-quenched samples as measured by EDS and annealing conditions.

Measured composition	DSC annealing at 5 K min^{-1}	Full crystallization
$Sm_{2.4}Fe_{77.6}B_{20}$	—	900 °C/4 days
$Sm_{4.0}Fe_{76.0}B_{20}$	491 °C	900 °C/4 days
	600 °C	
	812 °C	
$Sm_{5.6}Fe_{74.4}B_{20}$	—	900 °C/4 days
$Sm_{7.2}Fe_{72.8}B_{20}$	750 °C	900 °C/4 days
	812 °C	

phase transformations of primary crystallization products, is observed. The temperatures of each exothermic event are presented in table 2. Taking into account the temperature values of the main exothermic processes, $T_{onset} \approx 535\,^{\circ}$C, $T_{cryst} \approx 559\,^{\circ}$C, $T_2 \approx 638\,^{\circ}$C and $T_3 \approx 777\,^{\circ}$C, respectively, the DSC heating of the sample $x = 4.0$ at.% has been stopped at three crystallization stages, i.e. 491 °C (before T_{onset}), 600 °C (after T_{cryst}) and 812 °C (end of the DSC heating)—see table 1—each stage giving thus a different annealed sample. The obtained samples were then studied by XRD in order to investigate the phase structure and to assign the exothermic events to the corresponding phases that appear during the crystallization process.

Figure 2 shows the XRD profiles for the three above-mentioned samples. It is obvious that at 491 °C the curve exhibits a broad peak, typical for the amorphous state, indicating that the sample has not reached the primary crystallization stage. Nevertheless, a very small peak corresponding to the (110) reflection of the bcc α-Fe is distinguishable. At 600 °C, the sample exhibits some large, less intense peaks, corresponding to both the α-Fe and the tetragonal Fe_3B crystalline phases. The intensities of the peaks related to the two phases are

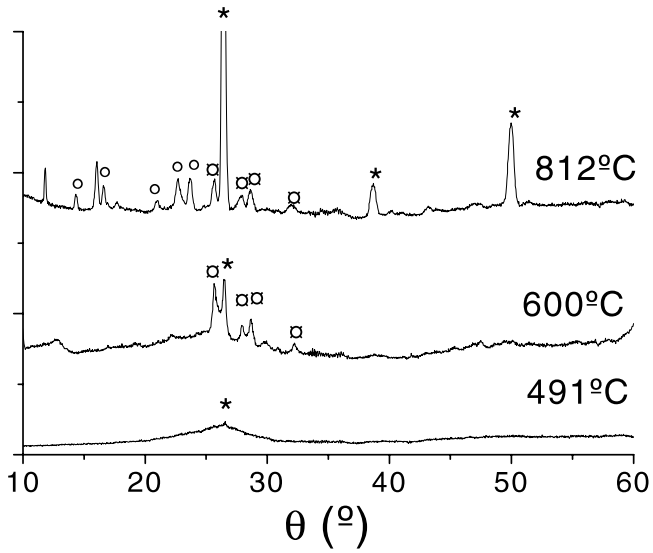

Figure 2. XRD profiles for the $x = 4.0$ at.% Sm ribbons after DSC annealing at 491, 600 and 812 °C. The symbols correspond to (∗) bcc α-Fe, (○) $Sm_{1.1}Fe_4B_4$ and (¤) tetragonal Fe_2B.

Table 2. The temperatures corresponding to the DSC events for all the annealed samples.

Measured composition	T_{onset} (°C)	T_{cryst} (°C)	T_2 (°C)	T_3 (°C)
$Fe_{77.6}Sm_{2.4}B_{20}$	421	459	624	800
$Fe_{76.0}Sm_{4.0}B_{20}$	535	559	638	777
$Fe_{74.4}Sm_{5.6}B_{20}$	563	585	630	754
$Fe_{72.8}Sm_{7.2}B_{20}$	—	673	715	—

rather comparable, pointing to an equal proportion of these phases. At the end of the DSC heating procedure (812 °C) the sample is fully crystallized, exhibiting sharp diffraction lines assigned to the α-Fe, Fe_3B and ternary $Sm_{1.1}Fe_4B_4$ phases. For 812 °C DSC annealing, the α-Fe becomes the preponderant phase in the composite sample. The relative intensities of the $Sm_{1.1}Fe_4B_4$ and Fe_3B phases are again rather comparable. The refinement of the XRD spectra allows one to determine the average particle size for the crystalline phases formed upon annealing. Following Scherrer's method [7], with the correction for instrumental broadening, the average particle size has been determined for the α-Fe and Fe_3B phases. The average particle sizes for the annealed samples are presented in table 3. As a general trend, one can observe that the particle size increases upon increasing the annealing temperature for both soft magnetic α-Fe and Fe_3B phases, evidencing the incipiency of crystallization at 491 °C with crystallites of about 2 nm and bigger crystallites at the end of DSC heating (around 6 nm for α-Fe and 11 nm for Fe_3B). It is worthwhile to observe that the ternary $Sm_{1.1}Fe_4B_4$ phase appears at the expense of Fe_3B whose relative amount decreases in the case of 812 °C DSC annealing compared with the 600 °C one. It could be inferred that the exothermic reactions observed at 638 and 777 °C could be respectively assigned to the phase decomposition of the metastable Fe_3B and the occurrence of the ternary $Sm_{1.1}Fe_4B_4$ phase.

In order to check this assumption, we have performed two DSC annealing treatments at the same heating rate of 5 K min^{-1} for the sample with Sm content $x = 7.2$ at.% up to 750

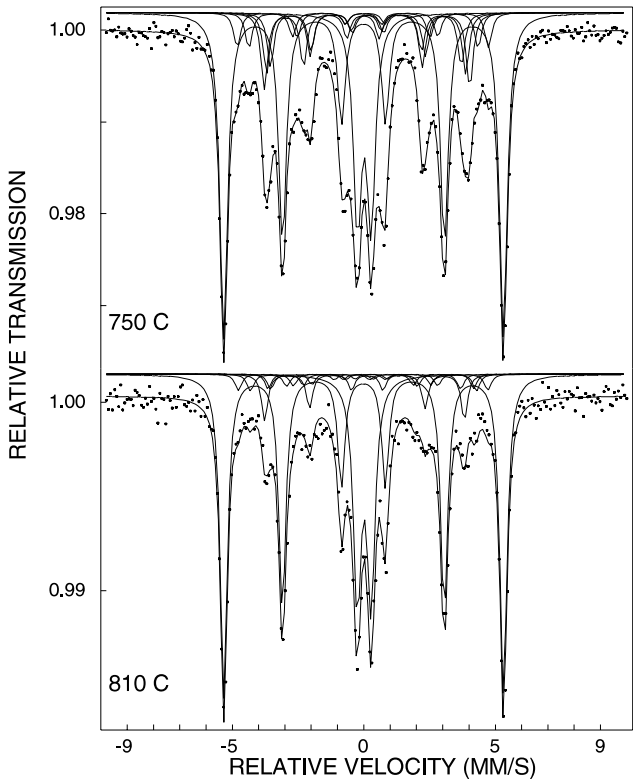

Figure 3. Room temperature Mössbauer spectra of $x = 7.2$ at.% Sm ribbons after DSC annealing at 750 and 810 °C.

Table 3. The average particle size of the soft magnetic phases developed after annealing, as resulted from XRD data.

Sample	Annealing	Particle size for α-Fe (nm)	Particle size for Fe_3B or Fe_2B (nm)
$Fe_{76.0}Sm_{4.0}B_{20}$	491 °C in DSC	2.3	—
	600 °C in DSC	4.7	8.2
	812 °C in DSC	6.4	10.9
$Fe_{76.0}Sm_{4.0}B_{20}$	900 °C/4 days	10.4	19.6
$Fe_{74.4}Sm_{5.6}B_{20}$	900 °C/4 days	10.8	21.1
$Fe_{72.8}Sm_{7.2}B_{20}$	900 °C/4 days	11.3	22.5

and 810 °C (above the two exothermic peaks, as seen in figure 1). The resulting samples were investigated by XRD and MS. The XRD spectrum for the sample annealed at 750 °C shows the presence of the following phases: α-Fe, Fe_3B, Fe_2B and $Sm_{1.1}Fe_4B_4$, while after 810 °C DSC annealing only the α-Fe and $Sm_{1.1}Fe_4B_4$ phases are detected. These results are confirmed by MS analysis. The corresponding Mössbauer spectra are shown in figure 3. The spectra were fitted with the magnetic sextets of the α-Fe, Fe_2B (two sextets) and Fe_3B (three sextets) phases and one paramagnetic doublet assigned to the $Sm_{1.1}Fe_4B_4$ phase. The corresponding Mössbauer parameters are shown in table 4. The proportions of the crystalline phases have been

Table 4. Hyperfine parameters of the contributions used to fit the room temperature Mössbauer spectrum of the $Sm_{7.2}Fe_{72.8}B_{20}$ ribbon subjected to DSC annealing up to 750 and 810 °C. (Note: the estimated errors are ±1% for relative proportion, ±0.02 mm s^{-1} for the linewidth and ±0.2 T for the hyperfine field.)

Sample	Contributions	Relative proportion (%)	Linewidth (mm s^{-1})	Hyperfine field (T)
$Sm_{7.2}Fe_{72.8}B_{20}$	α-Fe	49	0.36	33.1
annealed at	Fe_2B: I	8	0.30	23.6
750 °C	Fe_2B: II	10	0.30	24.4
	Fe_3B: I	5	0.30	29.7
	Fe_3B: II	5	0.30	22.6
	Fe_3B: III	7	0.30	27.2
	$Sm_{1.1}Fe_4B_4$	17	0.38	—
$Sm_{7.2}Fe_{72.8}B_{20}$	α-Fe	60	0.32	33.1
annealed at	Fe_2B: I	3	0.28	23.6
810 °C	Fe_2B: II	6	0.28	24.3
	Fe_3B: I	3	0.31	29.5
	Fe_3B: II	3	0.31	22.5
	Fe_3B: III	3	0.31	26.7
	$Sm_{1.1}Fe_4B_4$	22	0.36	—

calculated from the relative area of each Mössbauer contribution, assuming that the Lamb–Mössbauer factors of all the intermetallic crystalline phases are very close, as is generally the case for metallic alloys. One can observe a drastic decrease of the relative proportion of the borides (Fe_2B and Fe_3B) from around 35% for the 750 °C annealing down to 18% for the 810 °C annealing, at the benefit of α-Fe and ternary $Sm_{1.1}Fe_4B_4$ phase whose proportions increase from 49 to 60% for α-Fe and from 17 to 22% for $Sm_{1.1}Fe_4B_4$. These results, corroborated with the lack of formation of ternary metastable phases—such as cubic $Sm_3Fe_{62}B_{14}$, hexagonal $SmFe_{12}B_6$ or cubic $Sm_2Fe_{23}B_3$—as intermediate crystallization products, point to the fact that for a heating rate of 5 K min^{-1} there is one intermediate metastable phase, namely Fe_3B, and that the Sm ions randomly accommodate all the inequivalent Fe sites in the Fe_3B tetragonal structure, as has been already shown in our previous works [6, 8].

From these results, it can be concluded that, during the primary crystallization of the amorphous ribbons, both the α-Fe and Fe_3B phases simultaneously appear, while the higher temperature exothermic reactions correspond to the decomposition of the metastable Fe_3B phase into α-Fe and Fe_2B [8] and, respectively, to the formation of the ternary $Sm_{1.1}Fe_4B_4$ phase.

Nevertheless, by modifying the quenching parameters like quenching rate or thermal heating rate of the amorphous ribbons it is possible to overcome the limits of formation of metastable phases in the time–temperature–phase transformation (TTT) diagrams and consequently to promote or to inhibit different metastable phases according to the kinetics of nucleation and growth. These metastable precursors may give rise to different magnetic phases of interest, i.e. different crystallization products after subsequent annealing.

3.2. Phase structure of fully crystallized ribbons

In order to achieve complete crystallization, the $Sm_xFe_{80-x}B_{20}$ ribbons with $x = 2.4$, 4.0 and 5.6 at.% were subjected to an annealing treatment at 900 °C for 4 days.

The XRD patterns of the resulting samples (figure 4) show sharp lines, typical for fully crystallized materials. The main indexed phases are bcc α-Fe and tetragonal Fe_2B. Very weak

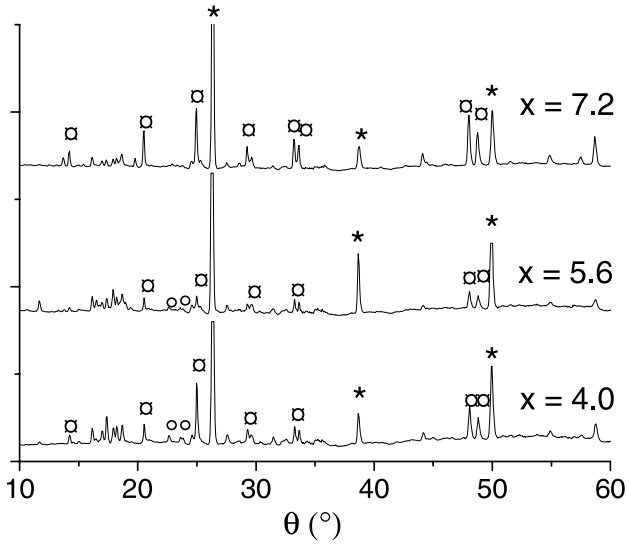

Figure 4. XRD profiles for ribbons with different Sm content, annealed at 900 °C for 4 days. The symbols correspond to (∗) bcc α-Fe, (O) $Sm_{1.1}Fe_4B_4$ and (¤) tetragonal Fe_2B.

lines corresponding to the tetragonal $Sm_{1.1}Fe_4B_4$ phase are also observed. As previously, from the Bragg peak linewidth, the average particle size for the main indexed phases (α-Fe and Fe_2B) have been derived and plotted in table 3. The average particle size is bigger than in the case of DSC annealed samples, because of the much higher heating rate, providing evidence for complete polymorphic crystallization of the samples. A slight increase of the average particle size for the two soft magnetic phases upon increasing the Sm content is observed. This is an indication of better thermal stability induced by the rare earth atoms in the molten state which in turn results in modifications of the crystalline structure and the magnetic interactions among these phases. In all the patterns, other peaks are observed that correspond to ternary Sm-containing phases, some of these peaks belonging to the tetragonal $Sm_2Fe_{14}B$ system. These results are sustained by the room temperature Mössbauer measurements. The room temperature Mössbauer spectra of the annealed ribbons are shown in figure 5. The spectra were fitted with the contributions of the bcc α-Fe (one sextet) and Fe_2B (two sextets) phases. An additional contribution (one sextet) was fitted, that is assigned to the ternary magnetic $Sm_2Fe_{14}B$ phase. In principle, the Mössbauer contribution of $Sm_2Fe_{14}B$ should be fitted with six magnetic sextets, corresponding to the six inequivalent Fe sites of the corresponding tetragonal phase. However, taking into account the complexity of the spectra for samples where up to four different phases co-exist, and the small relative proportion of the $Sm_2Fe_{14}B$ contribution, a fit with six magnetic sextets is meaningless. Consequently, one contribution with a hyperfine field equal to the mean value of the six magnetic sextets ($\approx$31 T) has been used. For the sample with Sm content $x = 2.4$ at.%, two other magnetic sextets were used for the fittings. These sextets could be assigned to the metastable $Sm_2Fe_{23}B_3$ phase, the assignment being based upon previous results of several authors. For example, Lewis and Panchanathan [9] have concluded that for boron/rare earth compositional ratio higher than one, as is the case for our samples, initial formation of complex boron-rich intermetallic metastable phases, such as $RE_2Fe_{23}B_3$, is promoted. The results of the fittings are shown in table 5. One can observe that the relative intensity of the α-Fe contribution increases with increasing Sm content while that of Fe_2B remains practically constant ($\approx$50%). The relative intensity of the $Sm_2Fe_{14}B$

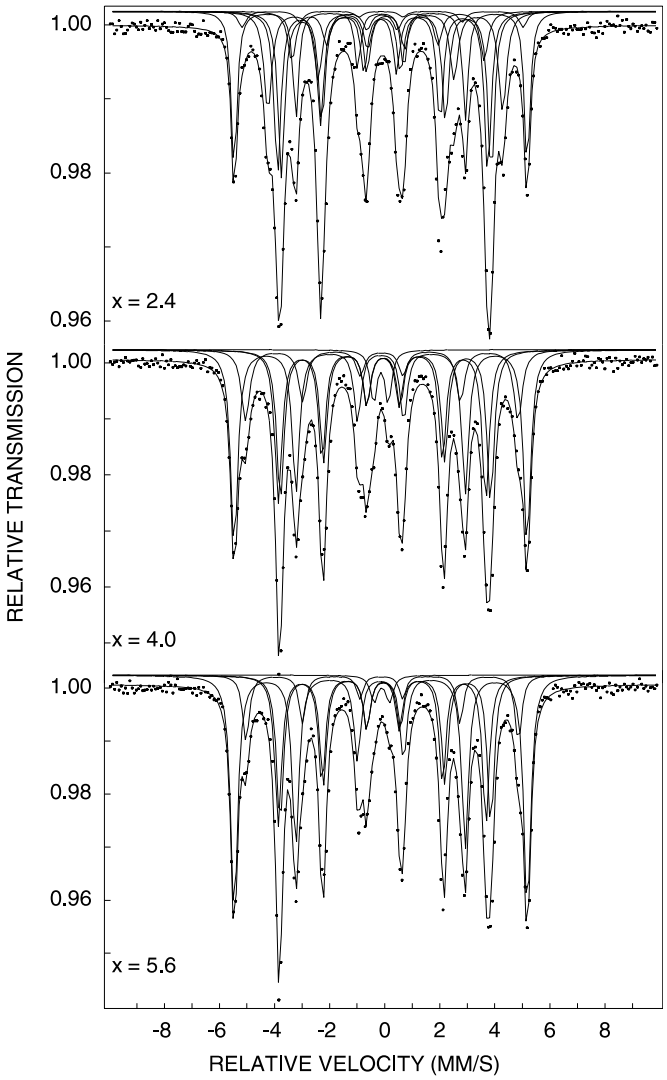

Figure 5. Room temperature Mössbauer spectra of ribbons with different Sm content, annealed at 900 °C for 4 days.

contribution is very small (3%) for the sample with $x = 2.4$ at.% and increases up to about 12–14% for the samples with higher Sm content, while the mean hyperfine field of this contribution does not vary significantly. A very small paramagnetic doublet (up to 4%) attributed to the $Sm_{1.1}Fe_4B_4$ was also included in the fittings for the samples with $x = 4.0$ and 5.6 at.%. It is worthwhile noticing that the hyperfine parameters obtained from the fit are consistent for each contribution considered over the whole set of measured samples. One can conclude that in fully crystallized $Sm_xFe_{80-x}B_{20}$ ribbons, with x smaller than a critical content of about 7 at.%, the soft magnetic Fe_2B and α-Fe phases are predominant and co-exist with the magnetic $Sm_2Fe_{14}B$ phase.

Table 5. Hyperfine parameters of the contributions used to fit the room temperature Mössbauer spectra of the fully crystallized ribbons. (Note: the estimated errors are ±1% for the relative proportion, ±0.02 mm s^{-1} for the linewidth, ±0.02 mm s^{-1} for the quadrupolar splitting QS or quadrupolar shift 2ε and ±0.2 T for the hyperfine field.)

Sample	Contributions	Relative proportion (%)	Linewidth (mm s^{-1})	QS, 2ε (mm s^{-1})	Hyperfine field (T)
$x = 2.4$	α-Fe	21	0.25	0.00	33.1
	$Sm_2Fe_{23}B_3$	17	0.34	−0.02	26.6
	$Sm_2Fe_{23}B_3$	9	0.34	0.08	21.8
	Fe_2B: I	25	0.29	0.01	24.1
	Fe_2B: II	25	0.29	0.04	23.3
	$Sm_2Fe_{14}B$	3	0.34	0.03	31.6
$x = 4.0$	α-Fe	32	0.31	0.00	33.1
	Fe_2B: I	25	0.31	0.02	24.2
	Fe_2B: II	25	0.31	0.00	23.2
	$Sm_{1.1}Fe_4B_4$	4	0.28	0.54	—
	$Sm_2Fe_{14}B$	14	0.37	0.00	30.8
$x = 5.6$	α-Fe	38	0.30	0.00	33.1
	Fe_2B: I	24	0.30	0.02	24.1
	Fe_2B: II	24	0.30	0.00	23.3
	$Sm_{1.1}Fe_4B_4$	2	0.32	0.56	—
	$Sm_2Fe_{14}B$	12	0.29	0.02	30.8

Table 6. Saturation magnetization σ_s and mean magnetic moment per grain μ obtained from the fit of the $\sigma(H)$ experimental data for fully crystallized ribbons to equation (1). The Bloch coefficient b and spin wave stiffness D are obtained from the fit of the $\sigma(T)$ experimental curves to equation (2).

Sm content (x) (at.%)	$\sigma_s(0)$ (emu g^{-1})	μ (μ_B)	b (10^{-6} $K^{-3/2}$)	D (meV Å^2)
2.4	228.7(9)	9380(60)	9.14(7)	156(1)
4.0	191.8(9)	8420(60)	7.4(18)	201(3)
5.6	184.7(9)	7460(60)	6.2(19)	232(3)

3.3. Magnetic properties of the fully crystallized ribbons

3.3.1. Field dependence of magnetization. The specific magnetization of the fully crystallized ribbons versus applied field (up to 5.5 T) was measured at 293 K for applied field parallel to the ribbon plane. The data exhibit typical ferromagnetic behaviour showing saturation below 1 T. It is known that for classical Heisenberg ferromagnets, the field dependence of the specific magnetization of an assembly of magnetic grains at a given temperature, T, can be written as

$$\sigma(H) = \sigma_s(0)L\left(\frac{\mu H}{k_B T}\right) \tag{1}$$

where $L(x) = \coth(x) - \frac{1}{x}$ is the Langevin function, $\sigma_s(0)$ the saturation magnetization, μ the mean magnetic moment per grain of the sample and H the applied field. The experimental data for the samples with Sm content $x = 2.4$, 4.0 and 5.6 at.% were fitted according to equation (1) with σ_s and μ as fitting parameters. The obtained values for σ_s and μ are summarized in table 6.

One can observe that on increasing the Sm content the saturation magnetization as well as the mean magnetic moment per grain decreases. The high value of saturation magnetization for $x = 2.4$ at.% is the result of phase structure of the sample which consist mainly of soft magnetic

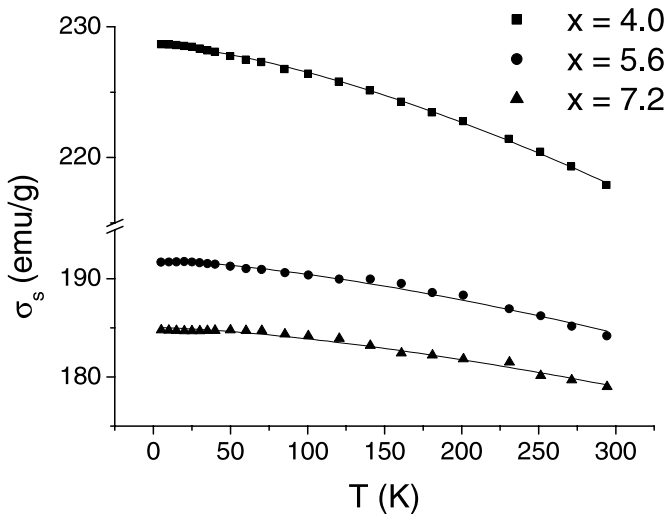

Figure 6. The specific magnetization versus temperature recorded for ribbons with different Sm content under an applied field of 1 kG. Full symbols: experimental curves; Line: the fit according to the Bloch's law—equation (2).

Fe_2B, α-Fe as well as metastable $Sm_2Fe_{23}B_3$ phases. Increasing the Sm content, the hard magnetic $Sm_2Fe_{14}B$ together with paramagnetic $Sm_{1.1}Fe_4B_4$ phases are formed (as indicated by MS analyses) and contribute to a subsequent decrease of the saturation magnetization of the sample. It is worth noticing that the exchange coupling of hard and soft magnetic regions within the crystallized samples governs the magnetic properties of the sample.

3.3.2. Spin wave excitations. It is well known [10] that the specific magnetization far below the Curie temperature of three-dimensional Heisenberg ferromagnets follows a Bloch law:

$$\sigma_s(T) = \sigma_s(0)(1 - bT^{3/2}) \tag{2}$$

where $\sigma_s(0)$ and $\sigma_s(T)$ are the values of the specific magnetization at 0 K and the temperature T, respectively, and b is the Bloch coefficient, expressed as

$$b = \varsigma(3/2)\frac{g\mu_B}{\sigma_s(0)\rho}\left(\frac{k_B}{4\pi D}\right)^{3/2} \tag{3}$$

where $\zeta(3/2) = 2.612$ is the Riemann function value in $3/2$, g the Landé factor, μ_B the Bohr magneton, ρ the density of the sample, k_B the Boltzmann constant and D the spin wave stiffness which expresses the excitations due to long-wavelength spin wave energy [11]. Experimental curves of the low-temperature dependence of magnetization, recorded under an applied field of 1 kG and plotted in figure 6, have been fitted according to equation (2). The values of b and D obtained from the fit are given in table 4. The values of the spin wave stiffness obtained from the fit are smaller than the value for the metallic iron (281 meV Å^2), as expected from the chemical composition of the precursor (about 75 at.% of Fe). It is worthwhile to notice that with increasing Sm content, the spin wave stiffness increases too. One should underline that spin wave excitations not only determine the low-temperature behaviour of the magnetization, but also account for the formation of the local inhomogeneous magnetization states [12]. From micromagnetic considerations the spin wave stiffness D is proportional to the exchange coupling via exchange stiffness constant A as defined in [12]. The increase of

the exchange coupling with increasing Sm content as a result of structural and morphological changes (increasing average particle size is an argument) of the samples is related to the formation of the $Sm_2Fe_{14}B$ magnetic phase. Enhanced exchange coupling between nanoscale magnetic regions corroborated with suitable arrangement of nanophases and inducing uniaxial anisotropy in order to optimize the magnetic properties would be a definite requirement for further applications as magnetic materials.

4. Conclusions

It has been shown that the crystallization process of the $Sm_xFe_{80-x}B_{20}$ melt spun amorphous ribbons is strongly dependent on the Sm content, mainly due to the influence of the Sm atoms on the local order of the originally amorphous alloys. During the crystallization process different intermediate metastable phases occur, depending on the chemical composition of the intermetallic alloy. Fully crystallized ribbons exhibit different crystallization products depending upon the Sm content. An Sm content higher than a critical value of about 7 at.% would lead to the formation of mainly α-Fe, Fe_2B and paramagnetic $Sm_{1.1}Fe_4B_4$ phases. For Sm content lower than 7 at.%, the promotion of undesired paramagnetic $Sm_{1.1}Fe_4B_4$ is inhibited and the fully crystallized samples contain a mixture of magnetic $Sm_2Fe_{14}B$, α-Fe and Fe_2B phases. Magnetic data have shown an increase of the exchange coupling related to the structural and morphological changes upon increasing the Sm content and the occurrence of the $Sm_2Fe_{14}B$ magnetic phase in agreement with the phase composition of the samples and average particle size determined from structural data. It is inferred that optimizing both the chemical composition by additional elements for inducing uniaxial anisotropy and the annealing procedures would lead to promising applications for the RE–Fe–B melt spun ribbons.

References

[1] Skomski R 1994 *J. Appl. Phys.* **76** 7059
[2] Fischer R, Schrefl T, Krönmuller H and Fidler J 1995 *J. Magn. Magn. Mater.* **150** 329
[3] Ravach G, Machizaud F, Teillet J, Le Breton J M and Fnidiki A 2000 *J. Phys.: Condens. Matter* **12** 3639
[4] Machizaud F, Ravach G, Teillet J and Le Breton J M 2000 *J. Phys.: Condens. Matter* **12** 8101
[5] Crisan O, Le Breton J M, Machizaud F, Labaye Y and Filoti G 2002 *J. Magn. Magn. Mater.* **242/245** 1297
[6] Jianu A, Crisan O, Kuncser V, Le Breton J M, Teillet J, Vasile E, Munteanu C and Filoti G 1997 *Mater. Sci. Eng.* A **226–228** 99
[7] Scherrer P 1918 *Nachr. Ges. Wiss. Gottingen* **2** 98
[8] Crisan O, Le Breton J M, Machizaud F, Jianu A, Teillet J and Filoti G 1998 *J. Physique* IV **8** 47
[9] Lewis L H and Panchanathan V 1999 *J. Appl. Phys.* **85** 4883
[10] Kaul S N 1981 *Phys. Rev.* B **24** 6550
[11] Brown W F (ed) 1963 *Micromagnetics* (New York: Wiley)
[12] Skomski R and Coey J M D (eds) 1999 *Permanent Magnetism* (Bristol: Institute of Physics Publishing)